

Estimation of land surface temperature–vegetation abundance relationship for urban heat island studies

Qihao Weng^{a,*}, Dengsheng Lu^{b,1}, Jacquelyn Schubring^a

^aDepartment of Geography, Geology, and Anthropology, Indiana State University, 200 North 7th Street, Terre Haute, IN 47809, USA

^bCenter for the Study of Institutions, Population, and Environmental Change, Indiana University, Bloomington, IN 47408, USA

Received 20 May 2003; received in revised form 5 November 2003; accepted 6 November 2003

Abstract

Remote sensing of urban heat islands (UHIs) has traditionally used the Normalized Difference Vegetation Index (NDVI) as the indicator of vegetation abundance to estimate the land surface temperature (LST)–vegetation relationship. This study investigates the applicability of vegetation fraction derived from a spectral mixture model as an alternative indicator of vegetation abundance. This is based on examination of a Landsat Enhanced Thematic Mapper Plus (ETM+) image of Indianapolis City, IN, USA, acquired on June 22, 2002. The transformed ETM+ image was unmixed into three fraction images (green vegetation, dry soil, and shade) with a constrained least-square solution. These fraction images were then used for land cover classification based on a hybrid classification procedure that combined maximum likelihood and decision tree algorithms. Results demonstrate that LST possessed a slightly stronger negative correlation with the unmixed vegetation fraction than with NDVI for all land cover types across the spatial resolution (30 to 960 m). Correlations reached their strongest at the 120-m resolution, which is believed to be the operational scale of LST, NDVI, and vegetation fraction images. Fractal analysis of image texture shows that the complexity of these images increased initially with pixel aggregation and peaked around 120 m, but decreased with further aggregation. The spatial variability of texture in LST was positively correlated with those in NDVI and in vegetation fraction. The interplay between thermal and vegetation dynamics in the context of different land cover types leads to the variations in spectral radiance and texture in LST. These variations are also present in the other imagery, and are responsible for the spatial patterns of urban heat islands. It is suggested that the areal measure of vegetation abundance by unmixed vegetation fraction has a more direct correspondence with the radiative, thermal, and moisture properties of the Earth's surface that determine LST.

© 2003 Elsevier Inc. All rights reserved.

Keywords: Land surface temperature; Vegetation abundance; Urban heat island; Spectral mixture analysis; Fractal analysis

1. Introduction

Urban climate studies have long been concerned about the magnitude of the difference in observed ambient air temperature between cities and their surrounding rural regions, which collectively describe the urban heat island (UHI) effect (Landsberg, 1981). Pertinent to the methods of temperature measurement, two types of UHI can be distinguished: the canopy layer (UCL) heat island, and the boundary layer (UBL) heat island (Oke, 1979). The former consists of air between the roughness elements, e.g., build-

ings and tree canopies, with an upper boundary just below roof level. The latter sits above the former, with a lower boundary subject to the influence of urban surface. UHI studies have traditionally been conducted for isolated locations and with in situ measurements of air temperatures. The advent of satellite remote sensing technology has made it possible to study UHI both remotely and on continental or global scales (Streutker, 2002). Studies on the UHI phenomenon using satellite derived land surface temperature (LST) measurements have been conducted primarily using NOAA AVHRR data (Balling & Brazell, 1988; Gallo et al., 1993; Gallo & Owen, 1998; Kidder & Wu, 1987; Roth et al., 1989; Streutker, 2002). The 1.1-km spatial resolution of these data is found suitable only for small-scale urban temperature mapping. The 120-m spatial resolution Landsat Thematic Mapper (TM) thermal infrared (TIR) data have also been utilized to derive surface temperatures. Carnahan

* Corresponding author. Tel.: +1-812-237-2255; fax: +1-812-237-8029.

E-mail addresses: geweng@isugw.indstate.edu (Q. Weng), dlu@indiana.edu (D. Lu).

¹ Tel.: +1-812-856-5767; fax: +1-812-855-2634.

and Larson (1990) used TM TIR data to observe meso-scale temperature differences between the urban and the rural area in Indianapolis. Kim (1992) studied the UHI phenomena in metropolitan Washington, DC, and pinpointed the significance of soil albedo and moisture availability to surface energy balance. Nichol (1994) carried out a detailed study using TM thermal data to monitor microclimate for housing estates in Singapore. Weng (2001, 2003) examined LST pattern and its relationship with land cover in Guangzhou and in the urban clusters in the Zhujiang Delta, China. Studies using satellite-derived radiant temperature have been termed as the surface temperature heat islands (Streutker, 2002). LST is believed to correspond more closely with the UCL heat islands, although a precise transfer function between LST and the near-ground air temperature is not yet available (Nichol, 1994). Byrne (1979) has observed a difference as much as 20 °C between the air temperature and the warmer surface temperature of dry ground. Because canopy layer may be discontinuous between urban structures, accurate representation of UHI requires high resolution of satellite imagery (Nichol, 1994). Streutker (2002, 2003) has recently successfully quantified the UHI of Houston, TX, as a continuously varying two-dimensional Gaussian surface superimposed on a planer rural background.

Research on LST shows that the partitioning of sensible and latent heat fluxes and thus surface radiant temperature response is a function of varying surface soil water content and vegetation cover (Owen et al., 1998). A higher level of latent heat exchange was found with more vegetated areas, while sensible heat exchange was more favored by sparsely vegetated such as urban areas (Oke, 1982). This finding encourages more and more research focusing on the relationship between LST and vegetation abundance (e.g., Carson et al., 1994; Gallo & Owen, 1998; Gillies & Carlson, 1995; Gillies et al., 1997; Goward et al., 2002; Lo et al., 1997; Weng, 2001), and using the relationship to derive biophysical parameters (Carson et al., 1994; Gillies & Carlson, 1995; Gillies et al., 1997) and to aid land cover mapping and change analysis (Lambin & Ehrlich, 1996; Sobrino & Raissouni, 2000).

In spite of these significant contributions, application of LST–vegetation abundance relationship to studies of UHI is rather limited. Using a Landsat ETM+ imagery of City of Indianapolis, IN, USA, this research aims to examine the surface temperature UHI in the city. Specific objectives of this research are: (1) to derive LST and analyze their spatial variations using Landsat ETM+ thermal measurements; (2) to apply linear spectral mixture analysis (LSMA) to estimate urban vegetation abundance; and (3) to investigate the relationship between LST and LSMA-derived vegetation abundance using conventional statistics and fractal analysis. This research will also investigate LST–NDVI relationship, so that the strengths and limitations of LSMA estimated vegetation fraction as compared to NDVI can be evaluated.

2. Background

2.1. Retrieval of LST

Satellite TIR sensors measure top of the atmosphere (TOA) radiances, from which brightness temperatures (also known as blackbody temperatures) can be derived using Planck's law (Dash et al., 2002). The TOA radiances are the mixing result of three fractions of energy: (1) emitted radiance from the Earth's surface, (2) upwelling radiance from the atmosphere, and (3) downwelling radiance from the sky. The difference between the TOA and land surface brightness temperatures ranges generally from 1 to 5 K in the 10–12- μm spectral region, subject to the influence of the atmospheric conditions (Prata et al., 1995). Therefore, atmospheric effects, including absorption, upward emission, and downward irradiance reflected from the surface (Franca & Cracknell, 1994), must be corrected before land surface brightness temperatures are obtained. These brightness temperatures should be further corrected with spectral emissivity values prior to the computation of LST to account for the roughness properties of the land surface, the amount and nature of vegetation cover, and the thermal properties and moisture content of the soil (Friedl, 2002). Two approaches have been developed to recover LST from multispectral TIR imagery (Schmugge et al., 1998). The first approach utilizes a radiative transfer equation to correct the at-sensor radiance to surface radiance, followed by an emissivity model to separate the surface radiance into temperature and emissivity (Schmugge et al., 1998). The second approach applies the split-window technique for sea surfaces to land surfaces, assuming that the emissivity in the channels used for the split window is similar (Dash et al., 2002). Land surface brightness temperatures are then calculated as a linear combination of the two channels. A major disadvantage of this approach is that the coefficients are only valid for the data sets used to derive them (Dash et al., 2002). In other words, a set of thermal responses for a specific landscape phenomenon or process measured using a specific TIR sensor cannot be extrapolated to predict the same TIR measurements either from other sensors, or from images recorded at different times using the same sensor (Quattrochi & Goel, 1995).

2.2. Emissivity

The effect of land surface emissivity on satellite measurements can be generalized into three categories: (1) emissivity causes a reduction of surface-emitted radiance; (2) non-black surfaces reflect radiance; and (3) the anisotropy of reflectivity and emissivity may reduce or increase the total radiance from the surface (Prata, 1993). Therefore, retrieval of LST from multispectral TIR data requires an accurate measurement of emissivity values of the surface (Caselles et al., 1995). The emissivity of a surface is controlled by such factors as water content, chemical composition, structure,

and roughness (Snyder et al., 1998). For vegetated surfaces, emissivity can vary significantly with plant species, areal density, and growth stage (Snyder et al., 1998). In the mean time, emissivity is a function of wavelength, commonly referred to as spectral emissivity (Dash et al., 2002). Estimation of emissivities for ground objects from passive sensor data has been measured using different techniques. Among these techniques are the normalized emissivity method (Gillespie, 1985), thermal spectral indices (Becker & Li, 1990), spectral ratio method (Watson, 1992), Alpha residual method (Kealy & Gabell, 1990), NDVI method (Valor & Caselles, 1996), classification-based estimation (Snyder et al., 1998), and the temperature emissivity separation method (Gillespie et al., 1998). These techniques are applicable to separate temperatures from emissivities, so that the effect of emissivity on estimated LST can be determined. Lack of knowledge of emissivity can introduce an error ranging from 0.2 to 1.2 K for mid-latitude summers and from 0.8 to 1.4 K for the winter conditions for an emissivity of 0.98 and at the ground height of 0 km, when a single channel method of LST estimation is used (Dash et al., 2002). Moreover, it may not be practical to measure emissivity values pixel-by-pixel, since numerous factors are involved. Snyder et al. (1998) proposed to use kernel methods applied to three bidirectional reflectance distribution function (BRDF) models (a geometric model for sparse vegetation, a volumetric model for dense vegetation, and a specular model for water and ice), so that each pixel can be categorized into 1 of the 14 emissivity classes based on conventional land cover classification and dynamic and seasonal factors.

2.3. Vegetation abundance and soil properties

Fractional vegetation cover depicts the amount and nature of vegetation cover, and modulates the proportions of vegetation and ground (e.g., bare soil) visible to a sensor. The differences in radiative temperature between the vegetation canopy and the ground affect the measurement of LST (Sandholt et al., 2002). For non-vegetated areas, LST measurements typically represent the radiometric temperatures of sunlit non-vegetated surfaces, such as bare soil. As the amount of vegetation cover increases, the radiative temperature recorded by a sensor approximates more closely the temperatures of green leaves, and the canopy temperature at spectral vegetation maximum or complete canopy cover (Goward et al., 2002). It is of significance to scrutinize the temperatures of each part of the vegetation-ground system (such as shaded ground, sunny ground, shade vegetation, and sunny vegetation) and to examine the effects of different canopy structures (Cassels et al., 1992a,b; Kimes, 1983). In general, for image pixels that are not completely occupied by a single homogenous vegetation or bare soil, LST measurements reflect a mixture of soil and vegetation canopy temperatures, resulting from a composite signature. The observed

portion of soil and vegetation can vary with the viewing angle, thus the amount of vegetation (ground) alters as the observation angle increases (Cassels et al., 1992a). In addition, LST measurement will also be subject to the influences of the lower atmosphere and the temperature difference between the vegetation canopy and the soil background (Friedl, 2002). Thermal responses for vegetation can be highly varied as a function of the biophysical properties of the vegetation itself as well (Quattrochi & Ridd, 1998).

For any surface material, certain internal properties, such as heat capacity, thermal conductivity and inertia, play important roles in governing the temperature of a body at equilibrium with its surroundings (Campbell, 2002). These thermal properties vary with soil type and its moisture content (Sandholt et al., 2002). Dry, bare, and low-density soils, for example, have been linked to high LST as a result of relatively low thermal inertia (Carnahan & Larson, 1990; Larson & Carnahan, 1997). The emissivity of soils is a function of soil moisture conditions, and soil density (Larson & Carnahan, 1997). Therefore, for areas characterized by partial vegetation cover, surface thermal properties can largely influence the measurement of LST through the thermal processes of conduction, convection, and radiation.

2.4. Relationship of NDVI with LST and vegetation abundance

The relationship between LST and vegetation indices, such as NDVI, has been extensively documented in the literature. The basis for using NDVI in LST estimation is that the amount of vegetation present is an important factor (Section 2.3), and NDVI can be used to infer general vegetation conditions. The combination of LST and NDVI by scatterplot results in a triangular shape (Carson et al., 1994; Gillies & Carlson, 1995; Gillies et al., 1997). The slope of the LST–NDVI curve has been related to soil moisture conditions (Carson et al., 1994; Gillies & Carlson, 1995; Gillies et al., 1997; Goetz, 1997; Goward et al., 2002), and the evapotranspiration of the surface (Boegh et al., 1998). Several methods have been developed to interpret the LST–NDVI space, including: (1) the ‘triangle’ method using soil–vegetation–atmosphere transfer (SWAT) model (Carson et al., 1994; Gillies & Carlson, 1995; Gillies et al., 1997); (2) in situ measurement method (Friedl & Davis, 1994); and (3) remote sensing based method (Betts et al., 1996). However, difficulties still exist in interpretation of LST for sparse canopies because the measurements have combined the temperature of the soil and that of the vegetation, and the combinations are often nonlinear (Sandholt et al., 2002).

The relationship between NDVI and fractional vegetation cover is not singular. Recent studies have shown that NDVI does not provide areal estimates of the amount of vegetation (Small, 2001). NDVI measurements are a function of the visible and near-infrared reflectance from plant

canopy, the reflectance of the same spectra from the soil, and the atmospheric reflectance, and are subject to the influence of an error related to observational and other errors (Yang et al., 1997). Plant species, leaf area, soil background, and shadow can all contribute to the NDVI variability (Jasinski, 1990). The relationship between NDVI and other measures of vegetation abundance (e.g., leaf area index values of larger than 3) is well known to be nonlinear (Asrar et al., 1984). This nonlinearity and the platform dependency suggest that NDVI may not be a good indicator for quantitative analyses of vegetation (Small, 2001), and the relationship between NDVI and LST needs further calibration. More quantitative, physically based measures of vegetation abundance are called for, especially for applications that require biophysical measures (Small, 2001). The importance of spatial resolution for detecting landscape patterns and changes should also be emphasized (Frohn, 1998), and the relationship between NDVI variability and pixel size should be further investigated (Jasinski, 1990).

3. Methods

3.1. Study area

The City of Indianapolis, located in Marion County, IN has been chosen as the area of study (Fig. 1). With over 0.8 million population, the city is the nation's 12th largest one. Situated in the middle of the country, Indianapolis

possesses several other advantages that make it an appropriate choice. It has a single central city, and other large urban areas in the vicinity have not influenced its growth. The city is located on a flat plain, and is relatively symmetrical, having possibilities of expansion in all directions. Like most American cities, Indianapolis is increasing in population and in area. The areal expansion is through encroachment into the adjacent agricultural and nonurban land. Certain decision-making forces have encouraged some sectors of Metropolitan Indianapolis to expand faster than others. Detecting its urban expansion and the relationship to UHI development is significant to understand, control, and plan the city's future development.

3.2. Image pre-processing

Landsat 7 Enhanced Thematic Mapper Plus (ETM+) image (Row/Path: 32/21) dated on June 22, 2000 was used in this research. The data acquisition date has a highly clear atmospheric condition, and the image was acquired through the USGS Earth Resource Observation Systems Data Center, which has corrected the radiometric and geometrical distortions of the images to a quality level of 1G before delivery. The Landsat image was further rectified to a common Universal Transverse Mercator coordinate system based on 1:24,000 scale topographic maps, and was resampled using the nearest neighbor algorithm with a pixel size of 30 by 30 m for all bands including the thermal band. The resultant RMSE was found to be less than 0.5 pixel.

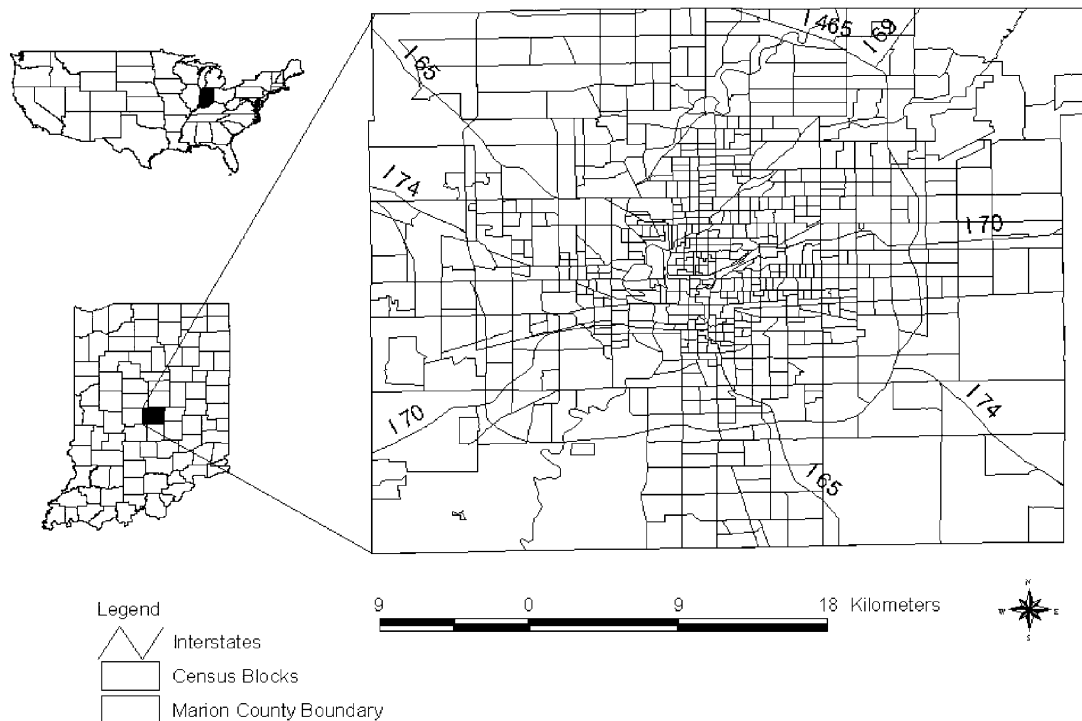


Fig. 1. A map of the study area.

3.3. Estimation of vegetation abundance using LSMA

LSMA is a physically based image processing method. It assumes that the spectrum measured by a sensor is a linear combination of the spectra of all components within the pixel (Adams et al., 1995; Roberts et al., 1998). The mathematical model of LSMA can be expressed as:

$$R_i = \sum_{k=1}^n f_k R_{ik} + ER_i \quad (1)$$

where $i = 1, \dots, m$ (number of spectral bands); $k = 1, \dots, n$ (number of endmembers); R_i is the spectral reflectance of band i of a pixel which contains one or more endmembers; f_k is the proportion of endmember k within the pixel; R_{ik} is the known spectral reflectance of endmember k within the pixel on band i ; and ER_i is the error for band i . A constrained least-squares solution was used in this research, assuming that the following two conditions are satisfied simultaneously:

$$\sum_{k=1}^n f_k = 1 \text{ and } 0 \leq f_k \leq 1 \quad (2)$$

$$\text{RMS} = \sqrt{\left(\sum_{i=1}^m ER_i^2 \right) / m} \quad (3)$$

Estimation of endmember fraction images with LSMA involves (1) image processing, (2) endmember selection, and (3) unmixing solution and evaluation of fraction images. Of these steps, selecting suitable endmembers is the most critical one in the development of high quality fraction images. Two types of endmembers can be applied: image endmembers, and reference endmembers. The former are derived directly from the image itself, while the latter are derived from field measurements or laboratory spectra of known materials (Roberts et al., 1998). For most remote sensing applications, image endmembers are utilized since they are easily obtained and capable of representing the spectra measured at the same scale as the image data (Roberts et al., 1998). Image endmembers are derived from the extremes of the image feature space, based on the assumption that they represent the purest pixels in the image (Mustard & Sunshine, 1999; Roberts et al., 1998).

Prior to derivation of fraction images, the minimum noise fraction (MNF) transformation (Green et al., 1988) was performed to reduce data redundancy and correlations between spectral bands (bands 1–5 and 7). Previous research has shown that use of MNF transform can improve the quality of fraction images (Lu et al., 2002; Small, 2001; Van der Meer & de Jong, 2000; Wu & Murray, 2003). The first four components were retained for use in the LSMA models, while the last two components discarded due to the high proportion of noise content. According to our previous

research in this area, three endmembers (shade, green vegetation or GV, and dry soil) can effectively develop high quality fraction images (Lu & Weng, in press). These endmembers were initially identified from the ETM+ image based on fieldwork and high-resolution aerial photographs, and then the radiances of these initial endmembers were compared with the endmembers selected from the scatterplot of MNF1 and MNF2. The endmembers with similar MNF spectra at the extreme vertices of the scatterplots were selected. A constrained least-square solution was applied to unmix the MNF components into fraction images. The resultant fraction images were used for LULC classification via a hybrid procedure that combined maximum likelihood and decision tree algorithms (Lu & Weng, in press), and the GV fraction used for further analysis of S_t /vegetation abundance relationship. Seven land use and land cover (LULC) types were identified, including: (1) commercial and industrial urban land, (2) residential land, (3) cropland, (4) grassland, (5) pasture, (6) forest, and (7) water (Fig. 2). Transect lines were overlaid for fractal analysis, see Section 3.5).

3.4. Derivation of LST from Landsat ETM+ imagery

The LST were derived from the corrected ETM+ TIR band (10.44–12.42 μm). The ETM+ thermal band has a spatial resolution of 60 m, and the thermal imagery from Landsat 7 is generally well calibrated to ground truth data (Arvidson, 2002). The local time of satellite overpasses was in the morning (approximately 11:14 AM) (this was the best image available), so that the chance for detecting a weakened UHI is maximized. However, satellite detection of heat islands using thermal infrared sensors has demonstrated that the heat island intensity is greatest in the daytime and in warm season and least at the nighttime—the opposite to the UHI results based on the measurement of air temperatures (Roth et al., 1989). The selection of the June 22 image is therefore appropriate although not optimal. The following equation was used to convert the digital number (DN) of Landsat ETM+ TIR band into spectral radiance (Landsat Project Science Office, 2002):

$$L_\lambda = 0.0370588 \times \text{DN} + 3.2 \quad (4)$$

The next step is to convert the spectral radiance to at-satellite brightness temperature (i.e., blackbody temperature, T_B) under the assumption of uniform emissivity (Landsat Project Science Office, 2002). The conversion formula is:

$$T_B = \frac{K_2}{\ln\left(\frac{K_1}{L_\lambda} + 1\right)} \quad (5)$$

where T_B is effective at-satellite temperature in K, L_λ is spectral radiance in $\text{W}/(\text{m}^2 \text{ ster } \mu\text{m})$; and K_2 and K_1 are

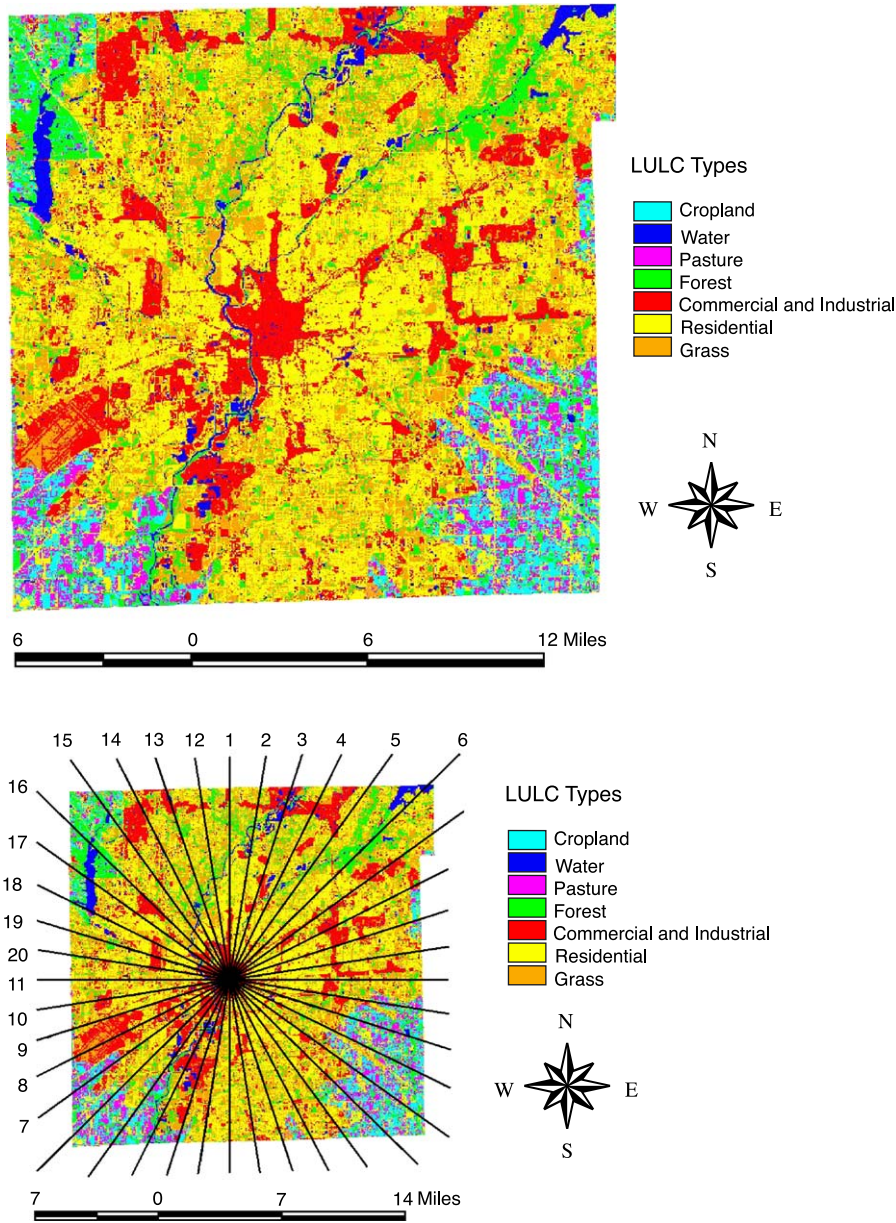


Fig. 2. Land use and land cover map in 2000. Transect lines are superimposed and numbered.

pre-launch calibration constants. For Landsat-7 ETM+, $K_2=1282.71$ K, and $K_1=666.09 \text{ mW cm}^{-2} \text{ sr}^{-1} \mu\text{m}^{-1}$.

The temperature values obtained above are referenced to a black body. Therefore, corrections for spectral emissivity (ϵ) became necessary according to the nature of land cover. Each of the LULC categories was assigned an emissivity value by reference to the emissivity classification scheme by Snyder et al. (1998). The emissivity corrected land surface temperatures (S_t) were computed as follows (Artis & Carnahan, 1982):

$$S_t = \frac{T_B}{1 + (\lambda \times T_B / \rho) \ln \epsilon} \quad (6)$$

where: λ = wavelength of emitted radiance (for which the peak response and the average of the limiting wavelengths

($\lambda = 11.5 \mu\text{m}$) (Markham & Barker, 1985) will be used), $\rho = h \times c / \sigma$ ($1.438 \times 10^{-2} \text{ m K}$), σ = Boltzmann constant ($1.38 \times 10^{-23} \text{ J/K}$), h = Planck's constant ($6.626 \times 10^{-34} \text{ Js}$), and c = velocity of light ($2.998 \times 10^8 \text{ m/s}$).

The NDVI image was computed from visible (0.63–0.69 μm) and near-infrared (0.76–0.90 μm) bands of the ETM+ image, so that the relationship between LST and NDVI can be studied.

3.5. Computation of fractal dimensions

Surface radiant emittance, as recorded by TIR sensors, includes both topographically and non-topographically induced high frequency variations such as roads and edges caused by different spectral characteristics of dif-

ferent neighboring land covers (Lam, 1990). The spatial surfaces generated from TIR image data therefore have a fractal characteristic that mixes topographic and non-topographic frequencies. The use of fractals for analyzing TIR images will improve our understanding of the thermal behavior of different land cover types, and the effect of landscape pattern on thermal environmental processes. Moreover, since remote sensing analysis of UHIs often involve multiple sensors, it will be critical to know if fractal dimension is predictable with changes in spatial and spectral resolutions. Previous studies have found fractals as an effective spatial measure for describing and analyzing remotely sensed imagery (De Cola, 1989; Emerson et al., 1999; Lam, 1990; Lam et al., 2002; Qiu et al., 1999; Weng, 2003).

To examine the spatial patterns of S_t , 20 transects (profiles) were drawn to across the image through the center of the city (Monument Circle), starting from the N–S profile (0° azimuth) and constructing a new transect every 18° (Fig. 2). Since these transects pass over various landscapes with different environmental settings, an inquiry into the fractal characteristics of the profiles will help to understand the factors shaping the city's thermal landscape and thus leading to the development of UHIs. These factors include the spatial pattern of different land cover classes, the occurrence of water bodies and parks, building and population densities, and the division of the city's functional districts, among others (Weng, 2003). The fractal dimension of these transects was estimated using the divider method. With this method, the total length of a curve/transect is plotted against the step size in a log–log form, and the fractal dimension D is estimated from the slope of the resulting regression model. Fig. 3 illustrates a self-affine fractal with a nominal length λ_0 digitized at discrete intervals of r and a standard deviation of heights

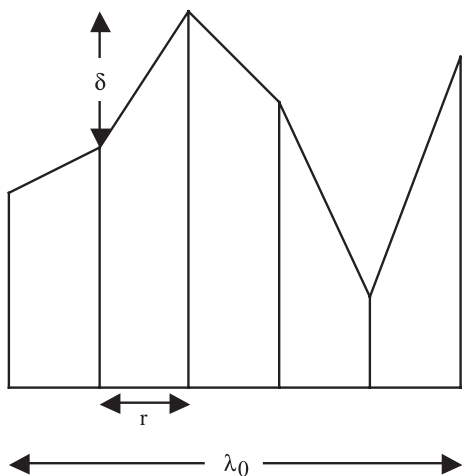


Fig. 3. Estimation of fractal dimension using the divider method. In the figure, δ is the standard deviation of surface height (average deviation from the mean) over a length scale r , and λ_0 is the total profile length (after Brown, 1995).

equal to δ , the total length of line α as a function of r is approximately:

$$\alpha = \frac{\lambda_0}{r} (r^2 + \delta^2)^{1/2} \quad (7)$$

For a self-affine fractal over distance r , the standard deviation of heights is:

$$\delta = b \left(\frac{r}{b} \right)^{2-D} \quad (8)$$

where b is the crossover length. It is interpreted as the horizontal sampling interval, above which the divider method breaks down. To obtain a meaningful result from the divider method, data must be digitized at a scale much smaller than the crossover length (Brown, 1995). Replace δ with the above expression, then Eq. (7) becomes

$$\alpha = \lambda_0 \left[1 + \left(\frac{r}{b} \right)^{2(1-D)} \right]^{1/2} \quad (9)$$

For $r \ll b$, $\log(\alpha)$ versus $\log(r)$ has slope of $1 - D$. When $r \gg b$, then $\alpha \approx \lambda_0$. In this case, calculating D by using the slope of the r – α curve gives $D \approx 1$.

The algorithm used for computation was originally developed by Goodchild (1980) and Shelberg et al. (1983), and elaborated in Lam (1990), Lam and De Cola (1993), and Jaggi et al. (1993). This algorithm measures the fractal dimension of isarithm lines characterizing a spatial surface, and averages the D values of all lines as the surface's final fractal dimension. The isarithm lines of a remotely sensed image are generated by dividing the range of the pixel values of the image into equally spaced intervals. The length of each isarithm, as represented by the number of edges, is then measured at various step sizes. The logarithm of the number of edges is regressed against the logarithm of the step sizes. The slope of the regression is obtained using a best-fit linear model, and thus a D value for the isarithm. A computer program was written for implementing the procedure.

4. Results

4.1. Characteristics of LST, NDVI, and vegetation fraction by land cover type

Fig. 4a shows the distribution of S_t values in Indianapolis. The radiant temperature ranged from 289.63 to 319.02 K with a mean of 302.14 K and standard deviation of 3.24. This choropleth map (Fig. 4a) was produced based on the classification scheme of standard deviation, in which class 1 data values are less than one standard deviation below the mean, class 2 values fall between the mean and one standard deviation below the mean, and so on (Smith, 1986). It is evident from the map that there is a thermal gradient as progressed from the Central Business District

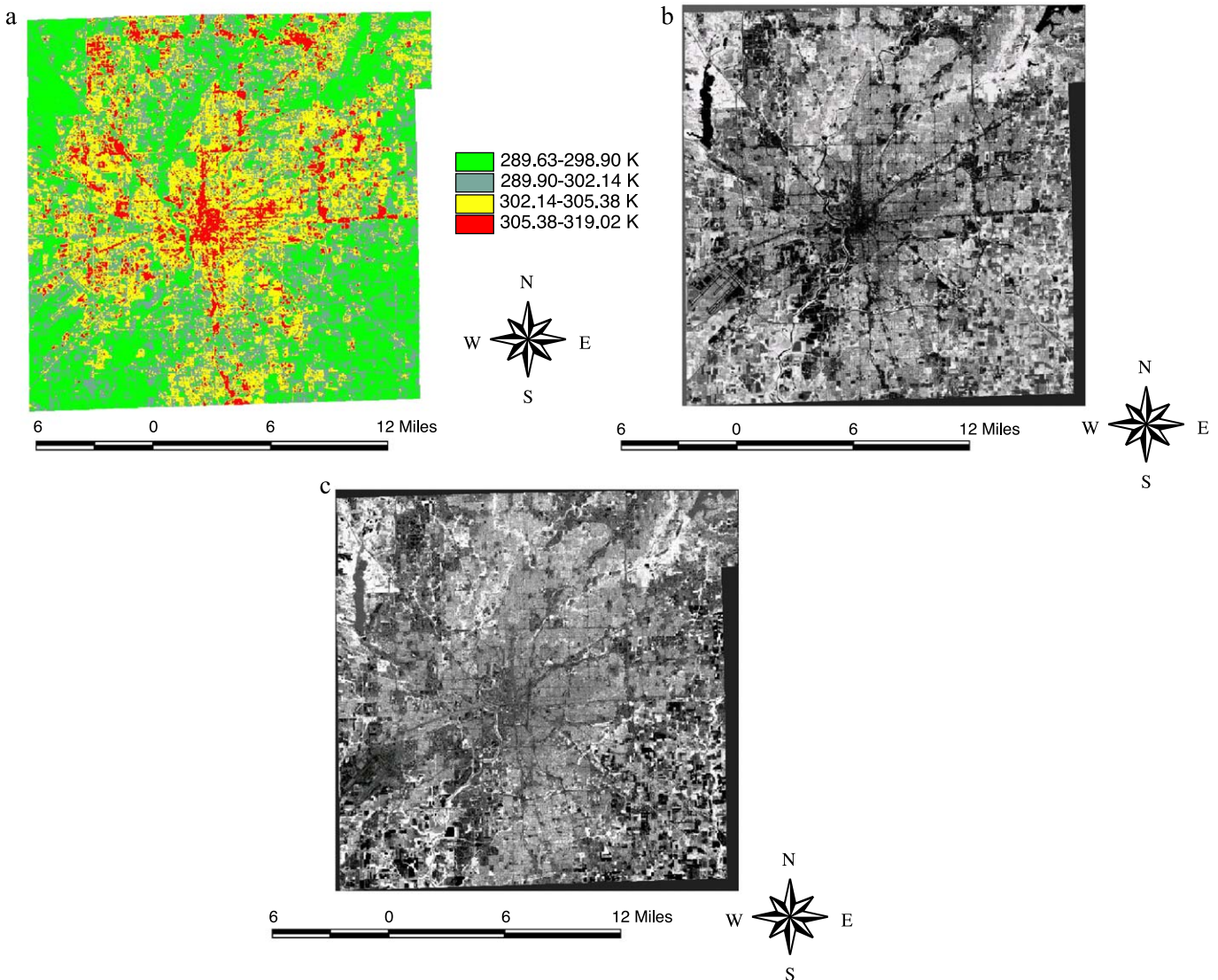


Fig. 4. Geographical distribution of land surface temperature (a), NDVI (b), and vegetation fraction (c).

(CBD) out into the countryside. Some hot spots, or urban heat islands, can be easily identified. The most extensive UHI was distributed in the central part of the CBD. There were also many smaller UHIs along Highway 465 (the bypass of the city shown in Fig. 1), in the north, west, and eastside of the city. However, there did not exist an extensive UHI in the southern part of the city, except for a few small ones along southward highways. Apparently, forest and agricultural uses in the southern part of the city contain the development of UHI. Interpreting thermal data and images of temperature distribution over an area is often not an easy job, because of many complex factors involved. The most influential factors for controlling the UCL heat island are the distribution of surface cover characteristics, and urban morphology, such as building materials, geometry, and density (Oke, 1982). Each component surface in urban landscapes exhibits a unique radiative, thermal, moisture, and aerodynamic properties, and relates to their sur-

rounding site environment. The myriad of the component surfaces and the spatial complexity when they mosaicked create a limitless array of energy balance and microclimate systems, confiscating urban meteorologists from drawing any generalization (Oke, 1982).

To better understand the relationship between S_t and land cover and thus vegetation abundance indicators (vegetation fraction, and NDVI), the thermal signature of each LULC type must be investigated. The statistics of S_t , NDVI, and vegetation fraction by LULC type were obtained by superimposing LULC image with images of S_t , NDVI, and vegetation fraction (Fig. 4a,b,c). The result of the GIS overlays is shown in Table 1. Column 1 of the table displays the mean and standard deviation values of S_t by LULC type. It is clear that commercial and industrial land exhibited the highest temperature (305.29 K), followed by residential land (303.80 K). The lowest temperature was observed in forest (298.16 K), followed by water bodies (298.20 K), and

Table 1
Descriptive statistics of biophysical parameters of the land cover types

Land use/cover type	Mean T_s (standard deviation)	Mean NDVI (standard deviation)	Mean vegetation cover (standard deviation)
Commercial and industrial	305.29 (3.10)	-0.193 (0.133)	0.119 (0.14)
Residential	303.80 (1.94)	0.088 (0.128)	0.276 (0.155)
Cropland	299.47 (1.28)	0.249 (0.22)	0.248 (0.333)
Grassland	300.47 (1.56)	0.335 (0.102)	0.37 (0.198)
Pasture	299.45 (1.04)	0.248 (0.109)	0.258 (0.166)
Forest	298.16 (1.37)	0.515 (0.06)	0.715 (0.104)
Water	298.20 (4.43)	-0.204 (0.25)	0.161 (0.178)

pasture (299.45 K). This implies that urban development brought up S_t by an average of 5.94 K by replacing natural environment (forest, water, and pasture) with non-evaporating, non-transpiring surfaces such as stone, metal, and concrete. The standard deviation value of S_t was large for commercial and industrial land (3.10 K), indicating that these surfaces experience a wide variation in S_t because of different construction materials. In contrast, the standard deviation value of S_t was relatively small for residential land (1.94 K) owing to their homogeneity. Furthermore, residential land possessed a smaller S_t mean value than commercial and industrial land, where buildings were frequently mixed with forest and grassland. The man-made vegetation cover, i.e., cropland and grassland, had an intermediate level of S_t (299.47 and 300.47 K, respectively), as they owned sparse vegetation and exposed bare soil. Forests showed a considerably lower S_t , because dense vegetation can reduce amount of heat stored in the soil and surface structures through transpiration. All vegetative cover, regardless of natural or man-made, exhibited an extremely small temperature variation. Water tended to get warm slowly during the summer owing to its rather high thermal inertia, and to convection and turbulence (e.g., wave action). Because of distinctive characteristics of rivers, lakes, reservoirs, and ponds, their S_t values vary, leading to a large standard deviation value of S_t for water (4.43 K).

Fig. 4b shows the distribution of NDVI values that vary from -0.606 to 0.651. The mean value for the image is 0.136, with the standard deviation of 0.245. Spatial variation of NDVI is not only subject to the influence of vegetation amount, but also to topography, slope, solar radiation availability, and other factors (Walsh et al., 1997). This image displays a large dark area (low values) at the center of the study area corresponding to the CBD of Indianapolis City. Bright areas of high NDVI values were found in the surrounding areas. Various types of crops were still at the early stage of growth or were before emergence, as indicated by medium gray to dark tone of the NDVI image in the

southeastern and southwestern parts of the study area. A similar geographic pattern of vegetation distribution can be detected in the vegetation fraction image (Fig. 4c), which has a range between -0.43 and 0.92, with a mean value of 0.286 and standard deviation of 0.24, respectively. A correlation analysis between the NDVI and the vegetation fraction images gives rise to a coefficient of 0.75, indicating a positive, moderately high correlation.

A closer look at the values of NDVI and vegetation fraction by LULC category (Table 1) indicates that the relationship between these two vegetation indicators may not be linear. In the vegetation fraction image (Fig. 4c), forest and dense grass appear very bright, while residential areas, pasture, and cropland appear grey, and urban areas and water appear dark. Forest exhibited the highest GV fraction value (mean=0.715), followed by grassland (0.37). This order is consistent with the NDVIs, which also shows the highest mean value in forest (0.515) and the second highest in grassland (0.335). However, for residential, pasture, cropland, commercial and industrial, and water, the order in GV fraction is different from that of NDVIs. Residential has the third highest GV fraction value of 0.276, but a small NDVI of 0.088. While cropland has a relatively high NDVI value (mean=0.249, third highest class), its GV fraction value (0.248) lags behind residential (0.276) and pasture (0.258). The lowest value of GV fraction was found in commercial and industrial land (mean=0.119), but in water in the NDVI image (-0.204). These differences reflect not only distinct computational procedures for deriving NDVI and GV fraction, but also their relations to true vegetation abundance, biomass, and vigor. Clearly, it is necessary to further examine the existing S_t and vegetation abundance relationship using GV fraction as an indicator.

4.2. Relationship between LST and vegetation abundance

The relationship between S_t and NDVI was investigated for each LULC type through correlation analysis (pixel by pixel). Table 2 shows the Pearson's correlation coefficients between the two variables at various resolution levels. The significance of each correlation coefficient was determined using a one-tail Student's *t*-test. It is apparent from Table 2 that S_t values tend to negatively correlate with NDVI values for all LULC types at all resolution levels. The highest negative correlation was found in cropland (-0.7265 at 30 m) and forest (-0.7156 at 30 m), followed by residential land (-0.6663 at 30 m) and commercial and industrial land (-0.6125 at 30 m). Pasture (-0.3363 at 30 m) and grassland (-0.3573 at 30 m) exhibited a moderately significant correlation. The lowest correlation was observed in water (-0.1972 at 30 m).

The strongest, negative correlation also existed between S_t and GV fraction values in cropland (-0.7538 at 30 m) and forest (-0.7343 at 30 m). The correlation coefficient values

Table 2
Correlation coefficients between S_t and GV fraction, and between S_t and NDVI by LULC type (significant at 0.05 level)

Resolution	30 m		60 m		120 m		240 m		480 m		960 m	
	S_t /GV fraction	S_t /NDVI	S_t /GV fraction	S_t /NDVI	S_t /GV fraction	S_t /NDVI	S_t /GV fraction	S_t /NDVI	S_t /GV fraction	S_t /NDVI	S_t /GV fraction	S_t /NDVI
Commercial and industrial land	-0.6559	-0.6125	-0.6630	-0.6244	-0.6729	-0.6360	-0.6694	-0.6107	-0.5863	-0.5594	-0.5430	-0.5217
Residential	-0.6763	-0.6663	-0.6897	-0.6812	-0.6909	-0.6845	-0.6875	-0.6365	-0.6003	-0.5619	-0.5862	-0.5449
Cropland	-0.7538	-0.7265	-0.7982	-0.7915	-0.8613	-0.8041	-0.8316	-0.7641	-0.7901	-0.7304	-0.7751	-0.6192
Grassland	-0.3760	-0.3573	-0.4431	-0.4056	-0.4856	-0.4149	-0.4546	-0.3934	-0.4097	-0.3382	-0.3656	-0.2911
Pasture	-0.4105	-0.3363	-0.4589	-0.4422	-0.4920	-0.4563	-0.4795	-0.4288	-0.4176	-0.3539	-0.3952	-0.3144
Forest	-0.7343	-0.7156	-0.7919	-0.7330	-0.8333	-0.7751	-0.7509	-0.7137	-0.7087	-0.6468	-0.6556	-0.5772
Water	-0.2416	-0.1972	-0.2601	-0.2587	-0.2719	-0.2707	-0.2219	-0.2178	-0.1935	-0.1887	-0.1130	-0.1027

dropped slightly for residential (-0.6763 at 30 m), and commercial and industrial land (-0.6559 at 30 m), with a sharp decrease for pasture (-0.4105 at 30 m) and grassland (-0.376 at 30 m). The least correlation was also found in water (-0.2416 at 30 m). By comparing NDVI's correlation and GV fraction's correlation coefficient values in Table 2, it is apparent that GV fraction values were more correlated with S_t . Since both vegetation indicators show the strong, negative correlation with land surface temperatures, it can be concluded that the higher biomass/vegetation abundance a land cover has, the lower the land surface temperature.

The 30-m S_t , NDVI, and GV fraction images were resampled to resolutions of 60, 120, 240, 480, and 960 m. Table 2 shows that the correlation coefficient values (between S_t and NDVI, and between S_t and GV fraction) vary across the spatial scales. The degree of correlation increases as pixel size increases up to a resolution level of 120 m, and then decreases with increasing pixel size. For example in cropland, correlation coefficient value between S_t and NDVI changes from -0.6725 (30 m), to -0.7915 (60 m), -0.8041 (120 m), -0.7641 (240 m), -0.7304 (480 m), and -0.6192 (960 m) as the pixels in the original NDVI image were averaged to the desired resolution level. Similarly, correlation coefficient between S_t and GV fraction in cropland reveals a continual increase from the values of -0.7538 (30 m), -0.7982 (60 m), and peaks at the resolution level of 120 m (-0.8613), and then slowly decreases to -0.8316 (240 m), -0.7901 (480 m), leveling out at the 960-m resolution to -0.7751. This pattern of changing correlation coefficient values is observed in all of the LULC categories (Table 2). The greatest, negative correlation always occur at the resolution level of 120 m, indicating the operational scales of S_t , NDVI, and GV fraction are around this spatial dimension (Lam & Quattrochi, 1992). Their relationships are best observed at the operational scales.

The strong correlation between S_t and vegetation abundance indicators in cropland and forest promise a potential success for using linear regression models to predict surface temperatures if NDVI and GV fraction values are known. The modeling results for cropland are displayed in Table 3. The multiple regression models are significant at 0.05 level. At the 120-m resolution, the multiple coefficient of determination, R^2 , is 0.7418, indicating that the predictor (GV fraction)

account for 74.18% of variance in the S_t distribution. The adjusted squared multiple R reduces this proportion to 0.735, a level expected when using this model in a new sample from the same population. If the NDVI is used as the predictor, the multiple coefficient of determination, R^2 , would be 0.6465, and the adjusted squared multiple R would be 0.6372. These results suggest that both GV fraction and NDVI are acceptable indicators of S_t .

4.3. Fractal analysis of LST and vegetation abundance

Fig. 5 shows S_t images at the resolutions ranging from 30 to 960 m. To examine the spatial patterns of S_t , 20 transects were drawn to across the image through the center of the city. To illustrate the distribution of S_t along

Table 3
Linear regression models for predicting S_t of cropland

Resolution	Model	Significance level	Coefficient of determination, R^2	Adjusted R^2
30 m	$Y = -2.69$ $\times X_{GV} + 299.79$	0.05	0.5682	0.5568
	$Y = -3.63$ $\times X_{NDVI} + 300.12$	0.05	0.4522	0.4378
60 m	$Y = -5.02$ $\times X_{GV} + 300.66$	0.05	0.6371	0.6276
	$Y = -3.07$ $\times X_{NDVI} + 300.14$	0.05	0.6265	0.6166
120 m	$Y = -3.47$ $\times X_{GV} + 299.81$	0.05	0.7418	0.7350
	$Y = -4.72$ $\times X_{NDVI} + 300.22$	0.05	0.6465	0.6372
240 m	$Y = -5.41$ $\times X_{GV} + 300.57$	0.05	0.6916	0.6835
	$Y = -3.19$ $\times X_{NDVI} + 300.01$	0.05	0.5838	0.5728
480 m	$Y = -4.98$ $\times X_{GV} + 300.25$	0.05	0.6243	0.6128
	$Y = -3.63$ $\times X_{NDVI} + 300.48$	0.05	0.5335	0.5207
960 m	$Y = -5.91$ $\times X_{GV} + 300.07$	0.05	0.6008	0.5903
	$Y = -2.77$ $\times X_{NDVI} + 300.01$	0.05	0.3835	0.3672

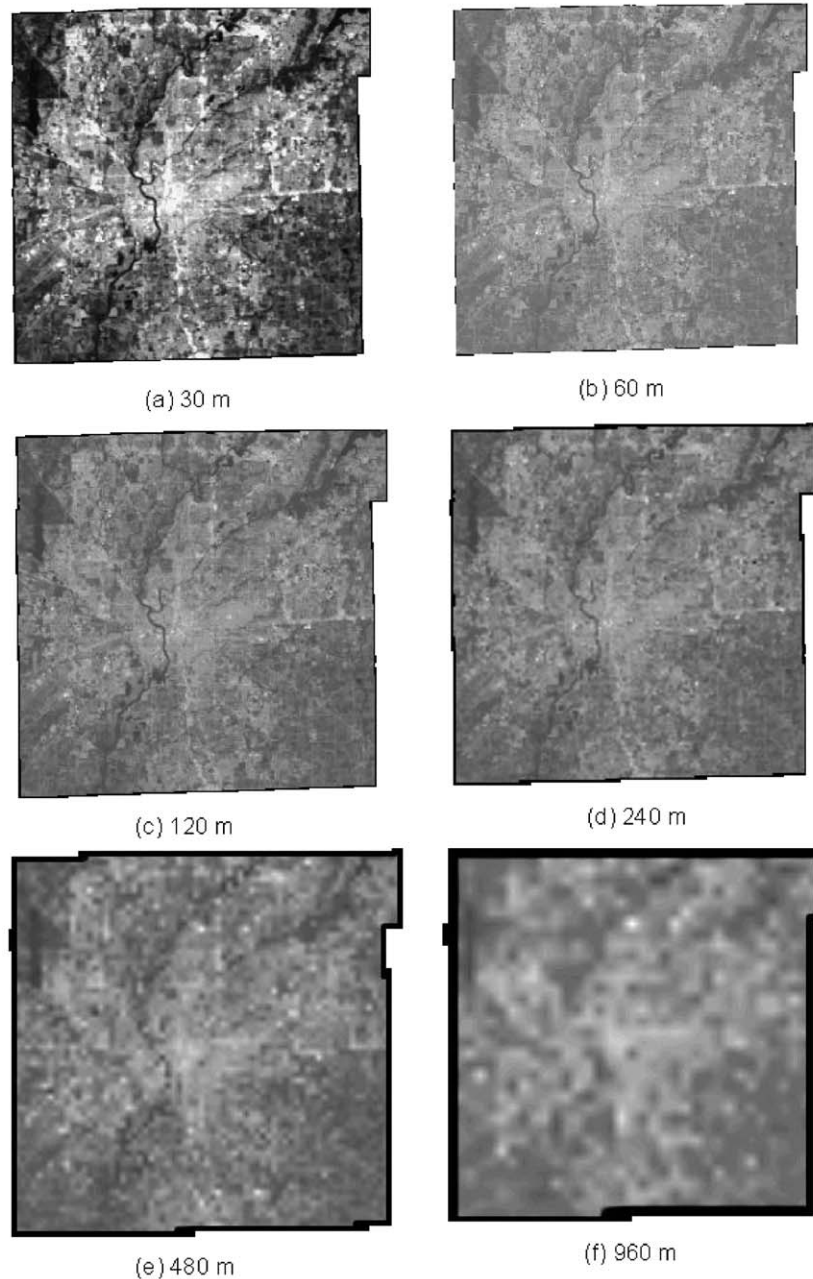


Fig. 5. Illustration of aggregated images of S_i . Present are an original image of 30-m resolution (a), and aggregated images at the resolutions of 60 (b), 120 (c), 240 (d), 480 (e), and 960 m (f).

the transects, the transect 11, i.e., the W–E temperature profile, was selected. Fig. 6 shows that the effect of convolving groups of small pixels into larger pixels has on the appearance of irregular surfaces. From the city's CBD area outward to the east and to the west, there exists a pronounced temperature gradient, as a result of the UHI effect. Numerous “peaks”, “valleys”, “plateaus”, and “basins” observable in Fig. 6a–f indicate that the heterogeneous nature of radiant temperature over the space. The calculated value of fractal dimension of this transect increases from 1.5014 at the 30 m resolution, to 1.503 and 1.5053 at the 60- and 120-m resolutions, respectively,

then declines with increasing pixel size (Table 4). A detailed examination of fractal dimensions of all transects shows a general pattern, i.e., with a few exceptions, the D values continuously increase with aggregation of pixel size up to 120–240 m, but decrease with further pixel aggregation. The response of fractal dimension to pixel aggregation as shown in Table 4 suggests that the spatial variability of radiant temperatures reaches the highest at the resolution ranging from 120 to 240 m. This scale of observation is related to the operational domain of the processes depicted in the input imagery (Cao & Lam, 1997; Lam & Quattrochi, 1992), i.e., the operational scale

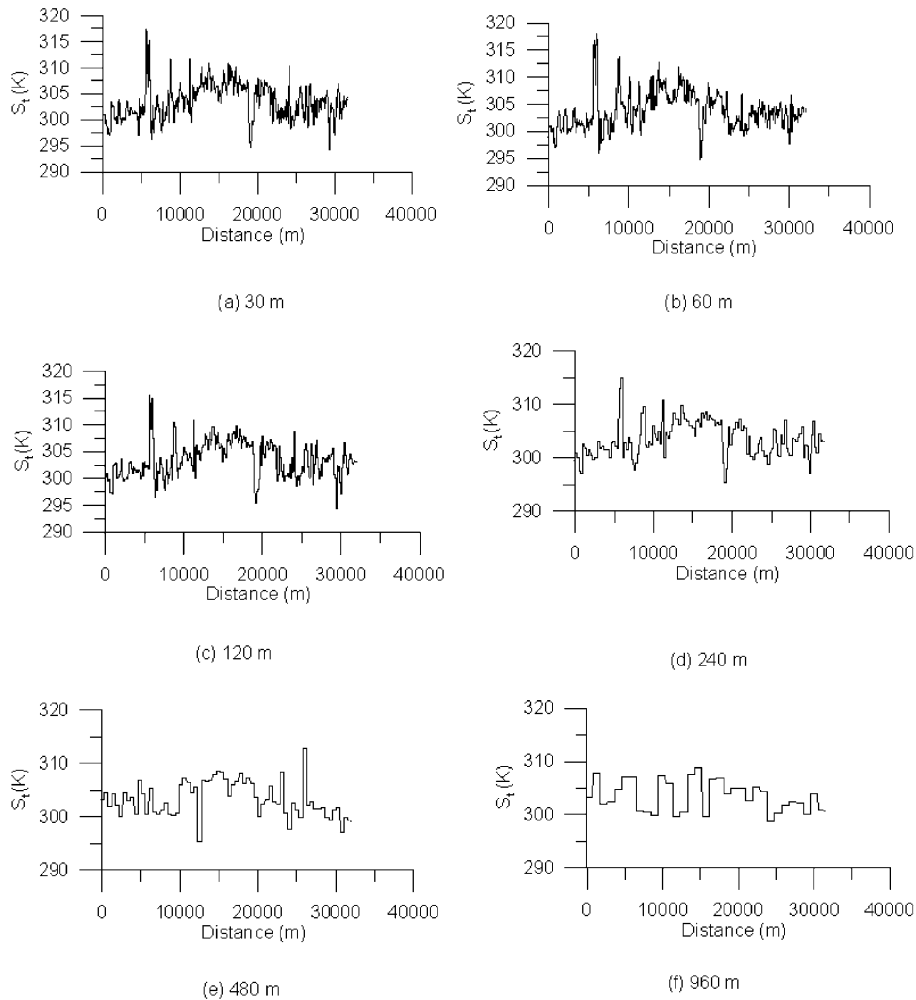


Fig. 6. Example of transects derived from the aggregated images of S_t (shown in Fig. 5). The variation of S_t along the transect #11 from West to East is displayed for the different resolutions.

where thermal landscape patterns (regulated by the factors identified above) are linked to processes in the study area. Beyond this point, thermal surfaces will become more spatially homogeneous and the textures less complex, as mixed pixels will smooth the distinction among different thermal responses. The fractal dimensions become more dependent of pixel size, and therefore less similar to the ideal fractal surfaces.

Transects exhibiting higher D values (such as Transects 4, 3, 6, and 16) are more spatially complex in texture than others. When a transect passes a large number of land cover patch of different types, or when the proportional distribution of patch types along a transect becomes more even, a higher spectral variability occurs among the neighboring pixels as a result of the spatial arrangement and areal extent of different land cover types. Previous studies have suggested that land use and land cover changes, especially urban development, will cause a greater contrast in the surface thermal properties, and thus an increase in fractal dimensions (Weng, 2003). Since urban development, such as constructions of buildings, roads,

highways, parks, and planting trees and grasses, tend to follow certain regular patterns, the superimposing of urban structures onto natural surfaces will increase the variability of radiant temperatures over the space, and result in higher fractal dimension values. However, an examination of Table 5 indicates that transects that pass over a large percentage of urban area, such as transects 8, 9, 10, and 12, yield a lower fractal dimensions. A correlation between the percentage of urban use (including commercial, industrial, and residential uses) and mean D values of the transects gives $r = -0.69$. This result indicates that when urban or built-up cover has occupied the majority of the surface, the thermal surface will become homogenized.

The vegetation fraction and NDVI transects generally have a lower value of fractal dimension than the S_t transects. The D value ranges from 1.0041 to 1.0118 for the vegetation fraction image, whereas the NDVI transects have fractal dimensionalities between 1.001 and 1.0158. The low values of fractal dimension for vegetation fraction and NDVI images are primarily due to the computation procedures and data normalization. NDVI is designed to capture the contrast

Table 4
Fractal dimensions of S_t across resolutions and their correlation with GV and NDVI (correlation significant at 0.05 level)

Transect #	Resolution						
	30 m	60 m	120 m	240 m	480 m	960 m	Mean
1	1.4707	1.4784	1.5101	1.5028	1.5026	1.4789	1.4906
2	1.4715	1.4771	1.4793	1.4853	1.4799	1.4754	1.4781
3	1.5414	1.5365	1.5526	1.5407	1.5264	1.5228	1.5367
4	1.53	1.5356	1.584	1.5514	1.5459	1.5319	1.5465
5	1.5162	1.519	1.5325	1.5221	1.511	1.4908	1.5153
6	1.5428	1.54	1.5544	1.5358	1.5271	1.5237	1.5373
7	1.513	1.5134	1.5175	1.5402	1.5043	1.5081	1.5161
8	1.4717	1.4722	1.4781	1.4991	1.4747	1.4519	1.4746
9	1.4201	1.448	1.4781	1.4578	1.4542	1.4314	1.4483
10	1.4563	1.4483	1.4732	1.4601	1.4446	1.4522	1.4558
11	1.5014	1.503	1.5053	1.4961	1.4833	1.4416	1.4885
12	1.5079	1.5109	1.5362	1.5156	1.5082	1.5035	1.5137
13	1.4917	1.4961	1.5047	1.4982	1.4921	1.4667	1.4916
14	1.4577	1.5024	1.511	1.4535	1.449	1.4578	1.4719
15	1.5044	1.5024	1.511	1.4971	1.4993	1.4907	1.5008
16	1.5542	1.5733	1.5851	1.5691	1.5635	1.5602	1.5676
17	1.5087	1.5108	1.5268	1.5098	1.5092	1.506	1.5119
18	1.5031	1.5233	1.5109	1.5171	1.5061	1.4966	1.5095
19	1.4954	1.5012	1.5337	1.5097	1.4995	1.4797	1.5032
20	1.532	1.5553	1.5558	1.5526	1.5067	1.4748	1.5295
S_t /GV correlation	0.6556	0.7967	0.8264	0.7980	0.7537	0.6808	
S_t /NDVI correlation	0.5422	0.5208	0.7743	0.6502	0.5793	0.5737	

between the red and infrared bands for vegetated pixels normalized by the sum of these bands. This normalization makes NDVI surfaces to become smoother, thus leading to lower D values than those computed from original spectral reflectance. In addition, because the index is constructed as a

ratio, it retains the ability to minimize topographic effects. The vegetation fraction is derived from a LSMA model based on the input from the first two components of MNF transformation, and the resultant fraction image represents the areal proportions of vegetation endmember within a pixel. A high degree of data normalization involves in the process of endmember selection and evaluation, and unmixing spectral images.

An examination of D values across spatial resolutions for vegetation fraction and NDVI images shows a pattern similar to that of S_t image. The D values, in both images, continuously increase with aggregation of pixel size up to 120–240 m, but decrease with further pixel aggregation. The impact of urban land cover on the fractal dimensions of individual transects is also evident in the vegetation fraction and NDVI images. The obvious relationship between the fractal dimensions of S_t and those of vegetation fraction and NDVI prompts the authors to conduct a correlation analysis. For the relationship between S_t and vegetation fraction, the correlation coefficient value ranges from 0.6556 to 0.8264 (Table 4). Varying with the level of pixel aggregation, the correlation yields the highest value at the 120-m resolution. Similarly, for the relationship between S_t and NDVI, the scale-dependent correlation has coefficient values in the range of 0.5208–0.7743, with the peak at the resolution of 120 m. Since fractals measure image texture, it can be concluded from these correlations that the spatial variability of texture in S_t is positively associated with those in the vegetation abundance indices. Because the development of the three image layers all involved to have referenced to or regulated by land cover types, the above finding has another important implication. The complexity of S_t , vegetation

Table 5
Land cover composition characteristics of the transects

Transect #	Percent of land cover						
	Cropland	Water	Pasture	Forest	Commercial and industrial	Residential	Grassland
1	0	1.58	0	5.01	32.69	42.53	18.19
2	0	4.01	0	4.36	25.37	47.78	18.48
3	1	8.28	1.34	5.52	41.89	28.01	13.96
4	1.02	7.43	0.7	9.3	27.05	35.26	19.23
5	3.96	4.52	7.07	9.96	23.82	33.14	17.53
6	5.54	4.59	4.91	14.1	19.19	39.9	11.77
7	4.13	1.85	5.56	4.92	32.29	36.49	14.75
8	0.4	0.96	0.32	1.92	36.67	38.51	21.22
9	0.43	1.19	1.28	2.04	33.87	43.91	17.28
10	0.09	1.23	0	2.65	23.1	52.82	20.11
11	0	3.19	0	3.19	23.43	47.38	22.8
12	0	1.22	0	5.6	32.37	38.85	21.96
13	0	1.6	0	8.19	25.65	42.28	22.28
14	0	2.38	0	5.88	24.88	46.9	19.95
15	4.37	2.26	2.77	8.45	17.92	39.04	25.2
16	8.07	1.88	7.93	16.28	20.74	34.38	10.72
17	8.79	5.58	7.51	6.00	19.44	39.60	13.08
18	5.21	4.19	4.74	10.9	20.14	41.00	13.82
19	7.59	2.02	8.6	7.76	22.77	37.61	13.66
20	3.85	1.75	5.86	6.56	30.33	39.51	12.15

fraction, and NDVI images is better characterized by non-topographically induced frequency variations resulted from different spectral characteristics of neighboring land covers. Image data derived according the procedures applied in this paper reveal less information on topographic frequencies. The reasonably high correlation between S_t , and vegetation fraction and NDVI at the most resolution levels assert that the vegetation abundance indices are good indicators of surface radiant temperatures, but vegetation fraction is a better one. The largest correlation coefficients observed at the resolution of 120 m in both cases further assert the operational scale of temperature variations is most likely to exist around the resolution of 120 m.

5. Discussions and conclusions

Vegetation abundance is one of the most influential factors in controlling LST measures through partitioning solar radiation into fluxes of sensible and latent heat and by limiting the proportions of vegetation and ground within a sensor's Instantaneous Field-of-View (IFOV). Studies on remotely sensed UHI in the past had exclusively used the NDVI as the indicator of vegetation abundance to estimate the LST–vegetation relationship. This study explores the usage of vegetation fraction derived from a spectral mixture model as a new indicator for the purpose of comparison. Results show that the unmixed vegetation fraction provides a slightly stronger negative correlation with LST for all land cover types at all levels of pixel aggregation. The LST–vegetation fraction relationship varies with the resolution, but yields the highest value around the resolution of 120 m. These findings suggest that the areal measure of vegetation abundance within a pixel has a more direct correspondence with the radiative, thermal, and moisture properties of the surface that determine LST. On the other hand, NDVI as a ratioing method can be especially useful because of the inverse relationship between vegetation brightness in the red and infrared region and the simplicity in computation. However, the NDVI does not measure the amount of vegetation, and its values can be influenced by many factors external to the plant leaf, including viewing angle, soil background, and differences in row direction and spacing in the case of agricultural crops. Further studies in the LST–NDVI relationship are necessary for non-vegetated or less-vegetated surfaces, including open water, man-made features, bare soil, and dead or stressed vegetation. In addition, since the NDVI measurement is dependent upon the spectral width of visible and near infrared band in a particular sensor, it will be difficult to extrapolate the results from a study to another. In contrast, unmixed vegetation fraction makes use of the full spectral reflectance vector of a sensor, and its values can be easily interpreted and applied. Clearly, there is a great promise for further studies on spectral

unmixing models and vegetation fraction as an UHI indicator.

Texture analysis of S_t , NDVI, and vegetation fraction images using the divider method of fractals indicates that the spatial complexity of the images alter with the resolutions. The general pattern of variation, as shown by fractal dimensions of the images, is that the complexity increases initially with aggregation of pixel size and peaks around 120 m, but decreases with further pixel aggregation. The spatial variability of texture in LST is positively correlated with those in NDVI and the unmixed vegetation fraction. The strongest association between LST and the two vegetation abundance indices occurs at the resolution of 120 m, where the maximum variability of texture is observed in the images. The fact that all the three images exhibit the largest differences in texture at the similar resolution level suggests that this observational scale reflects the operational processes in the images that interact to govern the landscape patterns and environmental processes of the study area. This spatial scale is roughly the length of a city block. Apparently, zoning, as a tool of urban planners, has a profound impact on the physical characteristics of urban landscapes by imposing such restrictions as maximum building height and density, the extent of impervious surface and open space, land use types and activities. These variables, in turn, control surface energy exchange, surface and subsurface hydrology, micro- to meso-scale weather and climate systems, and other environmental processes (Wilson et al., 2003). The operational scale observed in this study is in accordance with the scale suggested by Schmid (1988), who found that the directional variations of thermal radiance (i.e., effective anisotropy) could remain constant over a range of scales, which correspond to areas of similar urban structures that generate the regional homogeneity of LST, but the lower bound of the range may be 25 m (street/alley to house row spacing), 50 m (street to alley spacing), and up to 200 m in diameter. Urban surface anisotropy is expected to stay relatively constant as scales increase up to the limit where ground resolution begin to cover different land uses or surface structures, and the scale ranges from approximately 12 to 1000 m (Voogt & Oke, 1998).

Although many factors have contributed to the variations of spectral radiance and texture in LST, and thus to the spatial patterns of UHI, the spatial arrangement and areal extent of different land cover types is a fundamental one. As the sources and sinks for most of the material and energy movements and interactions between the geosphere and biosphere, changes in land covers will not only cause changes in physical quantities such as vegetative abundance and biomass, but also in thermal properties. The results from this study demonstrate that the interplay between thermal and vegetation dynamics creates unique signatures of these biophysical parameters in each land cover type, and further produce correlations among the images of LST, NDVI, and vegetation fraction. Since the texture complexity of these images is

modulated by non-topographically induced frequency variations, correlations in their fractal dimensions become apparent. Urbanization as a major LULC change process generally increases the spatial variability of LST, resulting in higher fractal dimension values. However, when urban structures and built-up area occupy the majority of a study area, its thermal surface will become spatially homogenized and the texture less complex. This preliminary result should not discourage studies in the effect of urban morphology on UHI, such as building materials, geometry, and density, which has been thought as another crucial factor in determining the reception and loss of radiation (Nichol, 1996; Oke, 1982). Since topography and morphology both have an effect on the measurement of fractal dimensionality from thermal surfaces, more research is desirable to apply height measurements and elevation data to the UHI studies.

The measurement of LST from thermal remote sensors can be far more complicated than the method presented here. Factors such as the scale-dependent nature of landscape characteristics, physiography, emissivity, atmospheric effects, and sensor-to-target noise have all contributed to the difficulties in the determination of LST at different spatial and temporal scales (Quattrochi & Goel, 1995). To obtain a reasonably high quality of estimates, four stages of correction process are required: (1) spectral radiance conversion to at-sensor brightness temperature; (2) correction for atmospheric absorption and re-emission; (3) correction for surface emissivity; and (4) correction for surface roughness. (Voogt & Oke, 2003). The effects of atmosphere and surface roughness on LST have not been taken into account in this study. Lack of atmospheric correction may introduce a temperature error of 4–7 °C for the mid-latitude summer atmosphere (Voogt & Oke, 1998). However, the horizontal variation could have been minimized because this study used an image acquired in a highly clear day and covering a small area. Errors due to urban effective anisotropy depend upon surface structure and relative sensor position, and can yield a temperature difference of up to 6 K or higher in downtown areas (Voogt & Oke, 1998). Effective LST can be derived only after its relationship to the component temperatures have been mathematically modeled (Cassels et al., 1992a,b; Kimes, 1983). Researches should be warranted in the future to determine the uncertainty in LST that resulted from different stages of the correction process and the impact of neglect or incorrect application of any correction procedure. These data uncertainties could alter our interpretations of LST patterns, and influence the calculation of fractal dimensions if they are applied. Factors such as solar illumination, the state of vegetation, atmospheric effect, land use and land cover pattern, and topography, all affect the fractal dimensionality from remotely sensed imagery (Weng, 2003). Further research is needed to differentiate the impact of each element, which holds great potential for characterization

of urban thermal landscapes and for planning and development of more advanced thermal infrared platforms.

Acknowledgements

The authors wish to thank anonymous reviewers for their constructive comments and suggestions. We further acknowledge the financial support of the University Research Committee at Indiana State University through the grant #UNR184 and the support from the Center for the Study of Institutions, Population, and Environmental Change (CIPEC), Indiana University, through the National Science Foundation (Grant 99-06826).

References

- Adams, J. B., Sabol, D. E., Kapos, V., Filho, R. A., Roberts, D. A., Smith, M. O., & Gillespie, A. R. (1995). Classification of multispectral images based on fractions of endmembers: Application to land cover change in the Brazilian Amazon. *Remote Sensing of Environment*, 52, 137–154.
- Artis, D. A., & Carnahan, W. H. (1982). Survey of emissivity variability in thermography of urban areas. *Remote Sensing of Environment*, 12, 313–329.
- Arvidson, T. (2002). Personal Correspondence, Landsat 7 Senior Systems Engineer, Landsat Project Science Office, Goddard Space Flight Center, Washington, DC.
- Asrar, G., Fuchs, M., Kanemasu, E. T., & Hatfield, J. L. (1984). Estimating absorbed photosynthetic radiation and leaf area index from spectral reflectance in wheat. *Agronomy Journal*, 76, 300–306.
- Balling, R. C., & Brazell, S. W. (1988). High resolution surface temperature patterns in a complex urban terrain. *Photogrammetric Engineering and Remote Sensing*, 54, 1289–1293.
- Becker, F., & Li, Z. -L. (1990). Temperature-independent spectral indices in TIR bands. *Remote Sensing of Environment*, 32, 17–33.
- Betts, A., Ball, J., Beljaars, A., Miller, M., & Viterbo, P. (1996). The land surface–atmosphere interaction: A review based on observational and global modeling perspectives. *Journal of Geophysical Research*, 101, 7209–7225.
- Boegh, E., Soegaard, H., Hanan, N., Kabat, P., & Lesch, L. (1998). A remote sensing study of the NDVI– T_s relationship and the transpiration from sparse vegetation in the Sahel based on high resolution satellite data. *Remote Sensing of Environment*, 69, 224–240.
- Brown, S. R. (1995). Measuring the dimension of self-affine fractals: Examples of rough surfaces. In C. C. Barton, & P. R. LaPointe (Eds.), *Fractals in the Earth Sciences* (pp. 77–87). New York: Plenum.
- Byrne, G. F. (1979). Remotely sensed land cover temperature and soil water status—a brief review. *Remote Sensing of Environment*, 8, 291–305.
- Campbell, J. B. (2002). *Introduction to Remote Sensing*. (3rd ed.). New York: The Guilford Press.
- Cao, C., & Lam, N. S. N. (1997). Understanding the scale and resolution effects in remote sensing and GIS. In D. A. Quattrochi, & M. F. Goodchild (Eds.), *Scale in Remote Sensing and GIS* (pp. 57–72). Boca Raton, FL: Lewis Publishers.
- Carnahan, W. H., & Larson, R. C. (1990). An analysis of an urban heat sink. *Remote Sensing of Environment*, 33, 65–71.
- Carson, T. N., Gillies, R. R., & Perry, E. M. (1994). A method to make use of thermal infrared temperature and NDVI measurements to infer surface soil water content and fractional vegetation cover. *Remote Sensing Reviews*, 9, 161–173.
- Cassels, V., Sobrino, J. A., & Coll, C. (1992a). On the use of satellite thermal data for determining evapotranspiration in partially vegetated areas. *International Journal of Remote Sensing*, 13, 2669–2682.

- Cassels, V., Sobrino, J. A., & Coll, C. (1992b). A physical model for interpreting the land surface temperature obtained by remote sensors over incomplete canopies. *Remote Sensing of Environment*, 39, 203–211.
- Caselles, V., Coll, C., Valor, E., & Rubio, E. (1995). Mapping land surface emissivity using AVHRR data: Application to La Mancha, Spain. *Remote Sensing Reviews*, 12, 311–3330.
- Dash, P., Gottsche, F. -M., Olesen, F. -S., & Fischer, H. (2002). Land surface temperature and emissivity estimation from passive sensor data: Theory and practice-current trends. *International Journal of Remote Sensing*, 23(13), 2563–2594.
- De Cola, L. (1989). Fractal analysis of a classified Landsat scene. *Photogrammetric Engineering and Remote Sensing*, 55, 601–610.
- Emerson, C. W., Lam, N. S. N., & Quattrochi, D. A. (1999). Multi-scale fractal analysis of image texture and pattern. *Photogrammetric Engineering and Remote Sensing*, 65, 51–61.
- Franca, G. B., & Cracknell, A. P. (1994). Retrieval of land and sea surface temperature using NOAA-11 AVHRR data in north-eastern Brazil. *International Journal of Remote Sensing*, 15, 1695–1712.
- Friedl, M. A. (2002). Forward and inverse modeling of land surface energy balance using surface temperature measurements. *Remote Sensing of Environment*, 79, 344–354.
- Friedl, M. A., & Davis, F. W. (1994). Sources of variation in radiometric surface temperature over a tallgrass prairie. *Remote Sensing of Environment*, 48, 1–17.
- Frohn, R. C. (1998). *Remote Sensing for Landscape Ecology*. Boca Raton, FL: Lewis Publishers.
- Gallo, K. P., McNab, A. L., Karl, T. R., Brown, J. F., Hood, J. J., & Tarpley, J. D. (1993). The use of NOAA AVHRR data for assessment of the urban heat island effect. *Journal of Applied Meteorology*, 32, 899–908.
- Gallo, K. P., & Owen, T. W. (1998). Assessment of urban heat island: A multi-sensor perspective for the Dallas-Ft. Worth, USA region. *Geocarto International*, 13, 35–41.
- Gillespie, A. R. (1985). Lithologic mapping of silicate rocks using TIMS. *Proceedings TIMS Data User's Workshop. JPL Publ.*, vols. 86–38 (pp. 29–44). Pasadena, CA: Jet Propulsion Laboratory.
- Gillespie, A. R., Rokugawa, S., Matsunaga, T., Cothem, J. S., Hook, S. J., & Kahle, A. B. (1998). A temperature and emissivity separation algorithm for advanced spaceborne thermal emission and reflection radiometer (ASTER) images. *IEEE Transactions on Geoscience and Remote Sensing*, 36, 1113–1126.
- Gillies, R. R., & Carlson, T. N. (1995). Thermal remote sensing of surface soil water content with partial vegetation cover for incorporation into climate models. *Journal of Applied Meteorology*, 34, 745–756.
- Gillies, R. R., Carlson, T. N., Cui, J., Kustas, W. P., & Humes, K. S. (1997). A verification of the 'triangle' method for obtaining surface soil water content and energy fluxes from remote measurements of the Normalized Difference Vegetation index (NDVI) and surface radiant temperature. *International Journal of Remote Sensing*, 18, 3145–3166.
- Goetz, S. J. (1997). Multisensor analysis of NDVI, surface temperature and biophysical variables at a mixed grassland site. *International Journal of Remote Sensing*, 18, 71–94.
- Goodchild, M. F. (1980). Fractals and the accuracy of geographical measures. *Journal of Mathematical Geology*, 12, 85–98.
- Goward, S. N., Xue, Y., & Czajkowski, K. P. (2002). Evaluating land surface moisture conditions from the remotely sensed temperature/vegetation index measurements: An exploration with the simplified simple biosphere model. *Remote Sensing of Environment*, 79, 225–242.
- Green, A. A., Berman, M., Switzer, P., & Craig, M. D. (1988). A transformation for ordering multispectral data in terms of image quality with implications for noise removal. *IEEE Transactions on Geoscience and Remote Sensing*, 26, 65–74.
- Jaggi, S., Quattrochi, D., & Lam, N. S. (1993). Implementation of operation of three fractal measurement algorithms for analysis of remote sensing data. *Computers and Geosciences*, 19, 745–767.
- Jasinski, M. F. (1990). Sensitivity of the Normalized Difference Vegetation Index to subpixel canopy cover, soil albedo, and pixel scale. *Remote Sensing of Environment*, 32, 169–187.
- Kealy, P. S., & Gabell, A. R. (1990). Estimation of emissivity and temperature using alpha coefficients. *Proceedings of Second TIMS Workshop. JPL Publ.*, vols. 90–95 (pp. 11–15). Pasadena, CA: Jet Propulsion Laboratory.
- Kidder, S. Q., & Wu, H. T. (1987). A multispectral study of the St. Louis area under snow-covered conditions using NOAA-7 AVHRR data. *Remote Sensing of Environment*, 22, 159–172.
- Kim, H. H. (1992). Urban heat island. *International Journal of Remote Sensing*, 13, 2319–2336.
- Kimes, D. J. (1983). Remote sensing of row crop structure and component temperatures using directional radiometric temperatures and inversion techniques. *Remote Sensing of Environment*, 13, 33–55.
- Lam, N. S. N. (1990). Description and measurement of Landsat TM images using fractals. *Photogrammetric Engineering and Remote Sensing*, 56, 187–195.
- Lam, N. S. N., & De Cola, L. (1993). *Fractals in Geography*. Englewood Cliffs, NJ: Prentice-Hall.
- Lam, N. S. N., & Quattrochi, D. A. (1992). On the issues of scale, resolution, and fractal analysis in the mapping sciences. *Professional Geographer*, 44, 88–98.
- Lam, N. S. N., Qiu, H., Quattrochi, D. A., & Emerson, C. W. (2002). An evaluation of fractal methods for characterizing image complexity. *Cartography and Geographic Information Science*, 29, 25–35.
- Lambin, E. F., & Ehrlich, D. (1996). The surface temperature-vegetation index space for land cover and land-cover change analysis. *International Journal of Remote Sensing*, 17, 463–487.
- Landsat Project Science Office (2002). Landsat 7 Science Data User's Handbook. URL: http://ftpwww.gsfc.nasa.gov/IAS/handbook/handbook_toc.html, Goddard Space Flight Center, NASA, Washington, DC (last date accessed: 10 September 2003).
- Landsberg, H. E. (1981). *The Urban Climate*. New York: Academic Press.
- Larson, R. C., & Carnahan, W. H. (1997). The influence of surface characteristics on urban radiant temperatures. *Geocarto International*, 12, 5–16.
- Lo, C. P., Quattrochi, D. A., & Luvall, J. C. (1997). Application of high-resolution thermal infrared remote sensing and GIS to assess the urban heat island effect. *International Journal of Remote Sensing*, 18, 287–304.
- Lu, D., Batistella, M., & Moran, E. (2002). Linear spectral mixture analysis of TM data for land-use and land-cover classification in Rondonia, Brazilian Amazon. In C. Armenakis, & Y. C. Lee (Eds.), *Proceedings of the ISPRS Commission IV Symposium: Geospatial theory, processing and applications* (pp. 557–562). Ottawa, Canada: Center for Topographic Information Mapping Services Branch, Geomatics Canada, Department of Natural Resources Canada.
- Lu, D., & Weng, Q. (in press). Spectral mixture analysis of the urban landscape in Indianapolis City with Landsat ETM+ imagery. *Photogrammetric Engineering and Remote Sensing*.
- Markham, B. L., & Barker, J. K. (1985). Spectral characteristics of the LANDSAT Thematic Mapper sensors. *International Journal of Remote Sensing*, 6, 697–716.
- Mustard, J. F., & Sunshine, J. M. (1999). Spectral analysis for earth science: Investigations using remote sensing data. In A. N. Rencz (Ed.), *Remote Sensing for the Earth Sciences: Manual of Remote Sensing* (3rd ed.), vol. 3 (pp. 251–307). New York: Wiley.
- Nichol, J. E. (1994). A GIS-based approach to microclimate monitoring in Singapore's high-rise housing estates. *Photogrammetric Engineering and Remote Sensing*, 60, 1225–1232.
- Nichol, J. E. (1996). High-resolution surface temperature patterns related to urban morphology in a tropical city: A satellite-based study. *Journal of Applied Meteorology*, 35, 135–146.
- Oke, T. R. (1979). *Technical Note No. 169: Review of Urban Climatology*, World Meteorological Organization, Geneva, Switzerland, 43 pp.
- Oke, T. R. (1982). The energetic basis of the urban heat island. *Quarterly Journal of the Royal Meteorological Society*, 108, 1–24.

- Owen, T. W., Carlson, T. N., & Gillies, R. R. (1998). An assessment of satellite remotely-sensed land cover parameters in quantitatively describing the climatic effect of urbanization. *International Journal of Remote Sensing*, 19, 1663–1681.
- Prata, A. J. (1993). Land surface temperatures derived from the advanced very high resolution radiometer and the along-track scanning radiometer: 1. Theory. *Journal of Geophysical Research*, 98, 16689–16702.
- Prata, A. J., Caselles, V., Coll, C., Sobrino, J. A., & Otle, C. (1995). Thermal remote sensing of land surface temperature from satellites: Current status and future prospects. *Remote Sensing Reviews*, 12, 175–224.
- Qiu, H. L., Lam, N. S. N., Quattrochi, D. A., & Gamon, J. A. (1999). Fractal characterization of hyperspectral imagery. *Photogrammetric Engineering and Remote Sensing*, 65, 63–71.
- Quattrochi, D. A., & Goel, N. S. (1995). Spatial and temporal scaling of thermal remote sensing data. *Remote Sensing Reviews*, 12, 255–286.
- Quattrochi, D. A., & Ridd, M. K. (1998). Analysis of vegetation within a semi-arid urban environment using high spatial resolution airborne thermal infrared remote sensing data. *Atmospheric Environment*, 32, 19–33.
- Roberts, D. A., Batista, G. T., Pereira, J. L. G., Waller, E. K., & Nelson, B. W. (1998). Change identification using multitemporal spectral mixture analysis: Applications in eastern Amazônia. In R. S. Lunetta, & C. D. Elvidge (Eds.), *Remote sensing change detection: Environmental monitoring methods and applications* (pp. 137–161). Ann Arbor, MI: Ann Arbor Sci. Publ.
- Roth, M., Oke, T. R., & Emery, W. J. (1989). Satellite derived urban heat islands from three coastal cities and the utilisation of such data in urban climatology. *International Journal of Remote Sensing*, 10, 1699–1720.
- Sandholt, I., Rasmussen, K., & Andersen, J. (2002). A simple interpretation of the surface temperature/vegetation index space for assessment of surface moisture status. *Remote Sensing of Environment*, 79, 213–224.
- Schmid, H.P. (1988). *Spatial Scales of Sensible Heat Flux Variability: Representativeness of Flux Measurements and Surface Layer Structure over Suburban Terrain*. PhD thesis. The University of British Columbia, Vancouver, BC.
- Schmugge, T., Hook, S. J., & Coll, C. (1998). Recovering surface temperature and emissivity from thermal infrared multispectral data. *Remote Sensing of Environment*, 65, 121–131.
- Shelberg, M. C., Lam, N. S. N., & Moellerling, H. (1983). Measuring the fractal dimensions of surfaces. *Proceedings of the Sixth International Symposium on Automated Cartography (Auto-Carto 6)*, Ottawa, Canada, vol. 2 (pp. 319–328). American Society for Photogrammetry and Remote Sensing (ASPRS).
- Small, C. (2001). Estimation of urban vegetation abundance by spectral mixture analysis. *International Journal of Remote Sensing*, 22, 1305–1334.
- Smith, R. M. (1986). Comparing traditional methods for selecting class intervals on choropleth maps. *Professional Geographer*, 38 (1), 62–67.
- Snyder, W. C., Wan, Z., Zhang, Y., & Feng, Y. -Z. (1998). Classification-based emissivity for land surface temperature measurement from space. *International Journal of Remote Sensing*, 19, 2753–2774.
- Sobrino, J. A., & Raissouni, N. (2000). Toward remote sensing methods for land cover dynamic monitoring: Application to Morocco. *International Journal of Remote Sensing*, 21, 353–366.
- Streutker, D. R. (2002). A remote sensing study of the urban heat island of Houston, Texas. *International Journal of Remote Sensing*, 23, 2595–2608.
- Streutker, D. R. (2003). Satellite-measured growth of the urban heat island of Houston, Texas. *Remote Sensing of Environment*, 85, 282–289.
- Valor, E., & Caselles, V. (1996). Mapping land surface emissivity from NDVI: Application to European, African, and South American areas. *Remote Sensing of Environment*, 57, 167–184.
- Van der Meer, F., & de Jong, S. M. (2000). Improving the results of spectral unmixing of Landsat Thematic Mapper imagery by enhancing the orthogonality of end-members. *International Journal of Remote Sensing*, 21, 2781–2797.
- Voogt, J. A., & Oke, T. R. (1998). Effects of urban surface geometry on remotely-sensed surface temperature. *International Journal of Remote Sensing*, 19, 895–920.
- Voogt, J. A., & Oke, T. R. (2003). Thermal remote sensing of urban climate. *Remote Sensing of Environment*, 86, 370–384.
- Walsh, S. J., Moody, A., Allen, T. R., & Brown, D. G. (1997). Scale dependence of NDVI and its relationship to mountainous terrain. In D. A. Quattrochi, & M. F. Goodchild (Eds.), *Scale in Remote Sensing and GIS* (pp. 27–55). Boca Raton, FL: Lewis Publishers.
- Watson, K. (1992). Spectral ratio method for measuring emissivity. *Remote Sensing of Environment*, 42, 113–116.
- Weng, Q. (2001). A remote sensing-GIS evaluation of urban expansion and its impact on surface temperature in the Zhujiang Delta, China. *International Journal of Remote Sensing*, 22, 1999–2014.
- Weng, Q. (2003). Fractal analysis of satellite-detected urban heat island effect. *Photogrammetric Engineering and Remote Sensing*, 69, 555–566.
- Wu, C., & Murray, A. T. (2003). Estimating impervious surface distribution by spectral mixture analysis. *Remote Sensing of Environment*, 84, 493–505.
- Wilson, J. S., Clay, M., Martin, E., Stuckey, D., & Vedder-Risch, K. (2003). Evaluating environmental influences of zoning in urban ecosystems with remote sensing. *Remote Sensing of Environment*, 86, 303–321.
- Yang, W., Yang, L., & Merchnat, J. W. (1997). An analysis of AVHRR/NDVI-ecoclimatological relations in Nebraska, USA. *International Journal of Remote Sensing*, 18, 2161–2180.